The Astrophysical Journal, 940:40 (8pp), 2022 November 20 https://doi.org/10.3847/1538-4357/ac9af2

The Active Galactic Nuclei in the Hobby–Eberly Telescope Dark Energy Experiment Survey (HETDEX). III. A Red Quasar with Extremely High Equivalent Widths Showing Powerful Outflows

Chenxu Liu[1], Karl Gebhardt[1], Wolfram Kollatschny[2], Robin Ciardullo[3,4], Erin Mentuch Cooper[1,5], Dustin Davis[1], Daniel J. Farrow[6,7], Steven L. Finkelstein[1], Eric Gawiser[8], Caryl Gronwall[3,4], Gary J. Hill[1,5], Lindsay House[1], Donald P. Schneider[3,4], Tanya Urrutia[9], and Gregory R. Zeimann[10]

[1] Department of Astronomy, The University of Texas at Austin, 2515 Speedway Boulevard, Austin, TX 78712, USA; lorenaustc@gmail.com
[2] Institut für Astrophysik, Universität Göttingen, Friedrich-Hund Platz 1, D-37077 Göttingen, Germany
[3] Department of Astronomy & Astrophysics, The Pennsylvania State University, University Park, PA 16802, USA
[4] Institute for Gravitation and the Cosmos, The Pennsylvania State University, University Park, PA 16802, USA
[5] McDonald Observatory, The University of Texas at Austin, 2515 Speedway Boulevard, Austin, TX 78712, USA
[6] University Observatory, Fakultät für Physik, Ludwig-Maximilians University Munich, Scheiner Strasse 1, D-81679 Munich, Germany
[7] Max-Planck Institut für extraterrestrische Physik, Giessenbachstrasse 1, D-85748 Garching, Germany
[8] Department of Physics and Astronomy, Rutgers, the State University of New Jersey, Piscataway, NJ 08854, USA
[9] Leibniz Institut für Astrophysik, Potsdam, An der Sternwarte 16, D-14482 Potsdam, Germany
[10] Hobby-Eberly Telescope, University of Texas, Austin, TX 78712, USA

Received 2022 July 1; revised 2022 September 29; accepted 2022 October 13; published 2022 November 18

Abstract

We report an active galactic nucleus (AGN) with an extremely high equivalent width (EW), $\mathrm{EW}_{\mathrm{Ly}\alpha+\mathrm{N\,V,rest}} \gtrsim 921$ Å, in the rest frame, at $z \sim 2.24$ in the Hobby–Eberly Telescope Dark Energy Experiment Survey (HETDEX), as a representative case of the high-EW AGN population. The continuum level is a nondetection in the HETDEX spectrum; thus the measured EW is a lower limit. The source is detected with significant emission lines ($>7\sigma$) at Lyα + N V λ1241, C IV λ1549, and a moderate emission line ($\sim 4\sigma$) at He II λ1640 within the wavelength coverage of HETDEX (3500–5500 Å). The r-band magnitude is 24.57 from the Hyper Suprime-Cam-HETDEX joint survey with a detection limit of $r = 25.12$ at 5σ. The Lyα emission line spans a clearly resolved region of $\sim 10''$ (85 kpc) in diameter. The Lyα line profile is strongly double peaked. The spectral decomposed blue gas and red gas Lyα emission are separated by $\sim 1\farcs2$ (10.1 kpc) with a line-of-sight velocity offset of ~ 1100 km s^{-1}. This source is probably an obscured AGN with powerful winds.

Unified Astronomy Thesaurus concepts: Active galaxies (17); Low-luminosity active galactic nuclei (2033); AGN host galaxies (2017)

1. Introduction

Active galactic nuclei (AGNs) are among the most energetic phenomena known in the universe. They can be identified with various observational techniques in different bands. Radio selection is sensitive to the powerful jet of luminous radio-loud AGNs. X-ray has strong penetration and low dilution from the host galaxies; thus it is the most efficient way to identify low-luminosity AGNs (e.g., Xue et al. 2016; Luo et al. 2017). Mid-IR can identify both obscured and unobscured AGN (e.g., Stern et al. 2012). However, different bands may represent different phases of AGN evolution and a single band identified AGN sample can be contaminated with strong starbursts. Deep UV/optical observations, especially the spectroscopic ones, are still a unique window to study the evolution of AGNs.

Traditional optical spectroscopic surveys of AGNs usually select targets based on photometric observations, i.e., detections in the broadband imaging with point-like morphologies to be distinguished from extended nearby galaxies, and blue colors to characterize the power-law continuum shape (e.g., Richards et al. 2006). The photometric selection can produce a selection effect on the AGN sample that fails to include the potential AGN population with optically faint host galaxies and high equivalent widths (EWs). These optically faint AGNs could either be intrinsically less massive, which could make them outliers in the supermassive black hole (SMBH)–host relation (see Kormendy & Ho 2013, for a review of the "coevolution" between SMBH and their host galaxies), or red and obscured AGNs.

Whether the coevolution stands for all SMBHs and their host galaxies remains an open question. Early works in the 1990s reported the discovery of "naked" quasars with no host galaxies (e.g., Bahcall et al. 1994). However, these "naked" quasars were later found to be hosted by normal elliptical galaxies with improved smoothing of the Hubble Space Telescope images (McIntosh et al. 1999; McLure et al. 1999). Simulations have suggested another special class of SMBHs that may not follow the SMBH–host correlation: the ejected SMBHs (Loeb 2007; Haiman et al. 2009; Ricarte et al. 2021). A SMBH binary in a gas-rich merger could be ejected as an SMBH remnant carrying an accretion disk. An SMBH remnant of an SMBH binary with similar masses could have a recoil speed of thousands of kilometers per second. The ejected SMBH could transverse a considerable distance from the merged galaxy and be observed as an off-centered quasar if the ejected SMBH happens to pass through a dense molecular cloud.

Red and obscured AGNs are very important candidates for understanding the early quasar phases, galaxy quenching, and the enrichment of the intergalactic medium (IGM). Interactions between galaxies can help remove the angular momentum of the cold gas in the outskirts of galaxies. The inflowed gas can fuel the star formation in the galaxies, feed the central SMBH, and trigger AGNs. The systems are then dusty, gaseous, and usually observed as red and obscured AGNs. The radiation from AGNs could in return power feedback and affect the evolution of their host galaxies. Strong outflows can clear up the gas reservoir in the host galaxies, shut down the star formation, enrich the environments, and make the AGN visible in optical. Outflows are widely used in understanding the coevolution between SMBHs and their host galaxies, the lack of luminous quasars in the luminosity function, and the quenching of the star formation of galaxies.

Spatially extended ionized gas and powerful outflow winds have been observed in a few high-redshift obscured quasars (Cai et al. 2017; Fluetsch et al. 2021; Vayner et al. 2021; Lau et al. 2022). These sources were preidentified in large surveys and followed up with hours of observation time for spatially resolved spectra on the Large Binocular Telescope/Medium-Dispersion Grating Spectroscopy, Keck/Keck Cosmic Web Imager, Very Large Telescope/Multi Unit Spectroscopic Explorer, etc.

In order to search for AGNs with high EWs, we need a spectroscopic survey that does not require continuum imaging preselection such as the Hobby–Eberly Telescope Dark Energy Experiment (HETDEX; Gebhardt et al. 2021). HETDEX is a spectroscopic survey with no photometric preselection (magnitude/color/morphology). All sources within the footprint of the survey are observed with a set of 78 integral field units consisting of 34,944 fibers and an 18 minute exposure. HETDEX enables spectroscopic detection of the AGNs hosted by galaxies that may be fainter than the detection limit of the corresponding photometric observations. Additionally, there is no need to perform follow-up observations for the extended sources on other instruments. The spatially resolved spectra can be obtained directly.

In this paper, we introduce an AGN (HETDEX J115031.93+504850.4, shortened to J1150+5048 in this paper) with an extremely high EW ($\mathrm{EW}_{\mathrm{Ly}\alpha+\mathrm{N\,V,rest}} \gtrsim 921\,\mathring{A}$) at $z \sim 2.24$ from the HETDEX survey. Section 2 briefly summarizes the first AGN catalog of the HETDEX survey. In Section 3 , we present the basic information of J1150+5048, why it is selected for study, and the detailed spatially resolved properties of J1150+5048 with its narrowband flux maps. We discuss the possible explanations for this high-EW AGN in Section 4. We summarize our discovery in Section 5.

2. The HETDEX AGN Catalog

HETDEX (Gebhardt et al. 2021) is an ongoing spectroscopic survey (3500–5500 Å) on the upgraded 10 m Hobby–Eberly Telescope (HET, Hill et al. 2021). It uses the Visible Integral field Replicable Unit Spectrograph (VIRUS; Hill et al. 2021) to record spectra of every object falling within its field of view. A typical exposure contains 34,944 spectra, most of which capture “blank” sky. The primary goal of this survey is to measure the large-scale structure at $z \sim 3$ using Lyα emitters (LAEs) as tracers. The HETDEX survey is expected to be active from 2017 to 2024, and eventually will cover 540 deg^2 with a filling factor of 1 in 4.6.

The first AGN catalog of the HETDEX survey is presented in Liu et al. (2022; Paper I). Here we briefly summarize the sample identification. AGN candidates are identified by requiring at least two significant AGN emission lines, such as the Lyα and C IV λ1549 line pair, or with a single broad emission line with FWHM > 1000 km s^{-1}, free of any preselection based on imaging (magnitude, morphology, or color). Each candidate AGN is then confirmed by visual inspection. This catalog contains 5322 AGN, covering an effective sky coverage of 30.61 deg^2 and a redshift range of $0.25 < z < 4.32$. Measurements from the overlap regions with the Hyper Suprime-Cam (HSC) imager of the Subaru telescope from the HSC-HETDEX joint survey (HSC-DEX; 5σ depth is $r \sim 25$ mag; S15A, S17A, S18A, PI: A. Schulze, and S19B, PI: S. Mukae) and the HSC Subaru Strategic Program (HSC-SSP; 5σ depth is $r \sim 26$ mag ; Aihara et al. 2019) show that the median r-band magnitude of our AGN catalog is 21.6 mag, with 34% of the objects having $r > 22.5$. Approximately 2.6% of the HETDEX AGN are not detected at >5σ confidence.

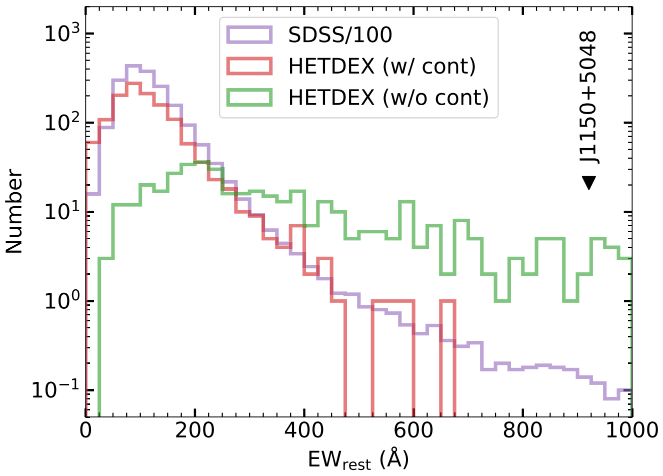

Figure 1. Distributions of the rest-frame EW of the Lyα + N V λ1241 emission. HETDEX AGNs with continuum detection (>1σ) are shown in the red histogram. HETDEX AGNs without continuum detection (<1σ) are shown in the green histogram. SDSS quasars are indicated by purple histogram. The number of SDSS quasars in each bin is divided by 100 for presentation purposes. $\mathrm{EW}_{(\mathrm{Ly}\alpha+\mathrm{N\,V}),\mathrm{rest}}$ of J1150+5048 is marked by the downward triangle.

3. J1150+5048

Figure 1 shows the distribution of the rest-frame EW of the Ly α + N V λ1241 emission of the HETDEX AGN with continuum detection (>1σ; red), that of the HETDEX AGN without continuum detection (<1σ; green), and that of the latest Sloan Digital Sky Survey (SDSS) quasar catalog (purple; Pâris et al. 2018; Rakshit et al. 2020). Similar with the SDSS quasars, the number of the HETDEX AGN detected with continuum decreases with $\mathrm{EW}_{(\mathrm{Ly}\alpha+\mathrm{N\,V}),\mathrm{rest}}$. The green histogram shows the distribution of the lower limits of $\mathrm{EW}_{(\mathrm{Ly}\alpha+\mathrm{N\,V}),\mathrm{rest}}$ for the HETDEX AGN not detected with continuum. In this paper, we study J1150+5048 as a representative case of the high-EW AGN population with no continuum detection as it is detected with significant emission lines (>7σ) at Lyα + N V λ1241, C IV λ1549, and a moderate emission line (∼4σ) at He II λ1640 (Figure 2). Additionally, it has very deep r-band imaging from HSC-DEX. It is a type-II AGN with narrow lines (FWHM < 1000 km s^{-1}). The fitting of the spectrum is detailed in Paper I. We fit a power-law continuum to the wavelength windows highlighted by the green shaded areas in Figure 2. The continuum subtracted emission lines are then fit with two Gaussian profiles if there is a significant broad component, otherwise a single narrow Gaussian profile is fit for each emission line.

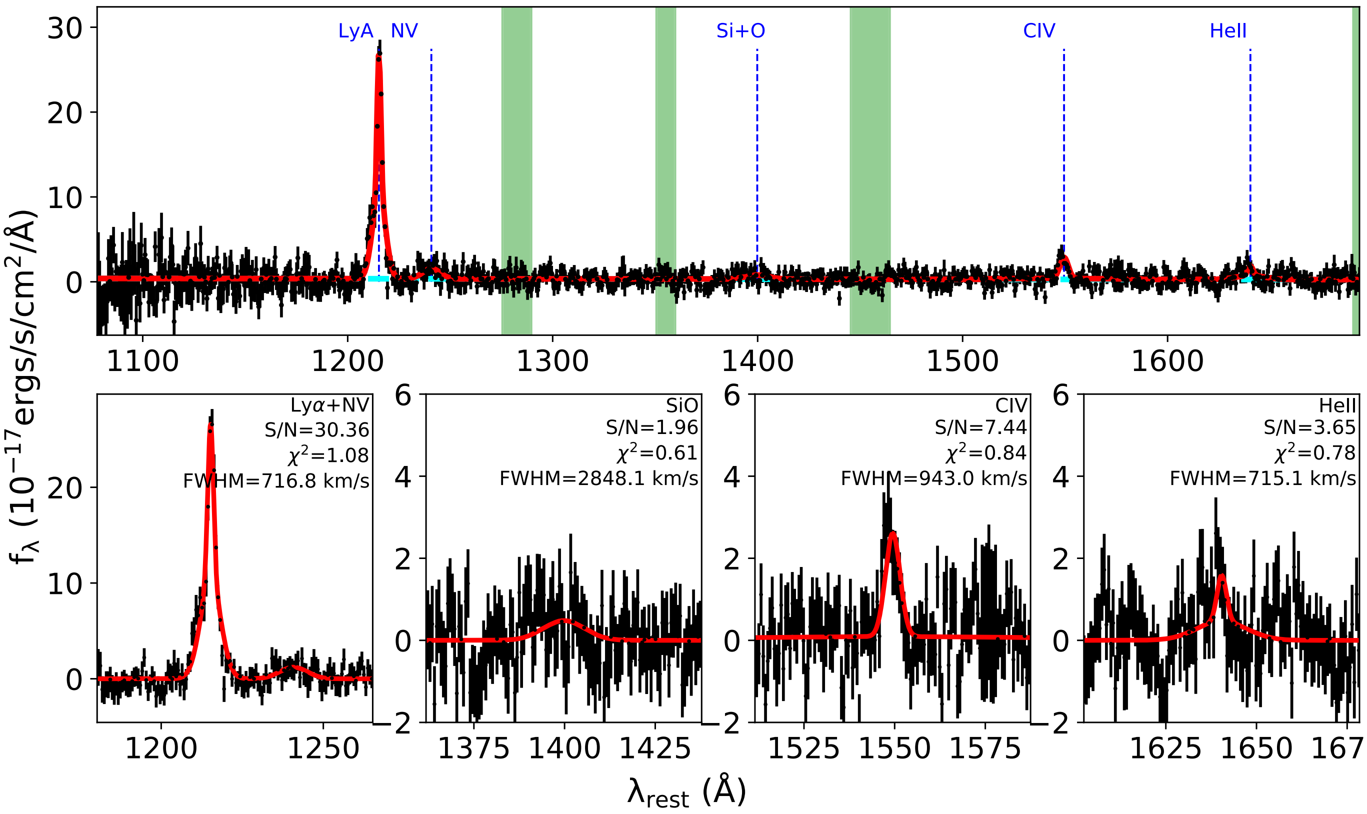

Figure 2. The HETDEX spectrum of J1150+5048 at the HETDEX coordinate in Table 1. Black data points with error bars are the observed spectrum shown in the rest frame. The red line is our best fit to the spectrum. The green shaded areas indicate the continuum windows used in the continuum fit. The cyan dashed line is our best-fit continuum model. The four panels in the bottom row are the continuum subtracted local areas of the four emission lines.

Table 1
Basic Information for J1150+5048

Coordinate					
(R.A., Decl.) (HETDEX)		(R.A., Decl.) (WISE)		Redshift	
(177.633030, 50.813999)		(177.632964, 50.814293)		2.24	
Rest-frame equivalent width (Å)					
$EW_{Ly\alpha}$	$EW_{N\ V}$	$EW_{Ly\alpha+N\ V}$	$EW_{Si\ IV+O\ IV]}$	$EW_{C\ IV}$	$EW_{He\ II}$
>747	>174	>921	⋯	>177	>86
Broadband Photometry					
g_{AB}	r_{AB}	$W1_{Vega}$	$W2_{Vega}$	$W3_{Vega}$	$W4_{Vega}$
>24.23	24.57 ± 0.13	17.50 ± 0.14	16.82 ± 0.29	12.47 ± 0.38	>8.93

Note. (1) The Rest-frame EWs are all lower limits, because the continuum level in the [1275, 1290] Å window at $(1.4 \pm 8) \times 10^{-18}$ erg s^{-1} cm^{-2} Å^{-1} used in the calculation of EWs is a nondetection. (2) g_{AB} is measured from the HETDEX spectrum (see D. Davis et al. 2022, in preparation for more details) at the HETDEX coordinate. The continuum of J1150+5048 is a nondetection in the g band. 24.23 is 1σ lower limit. (3) r_{AB} is measured from HSC-DEX at the WISE pointing. The 5σ depth of this field is $r = 25.12$ (AB mag). (4) W1 − W4 are taken from the ALLWISE catalog (Cutri et al. 2021). W1, W2, W3, and W4 are the filters at 3.4, 4.6, 12, and 22 μm, respectively. W4 is a nondetection.

Table 1 lists the basic information of J1150+5048. The EWs are measured directly from the ratio between the line flux and the best-fit continuum at the lines from the spectrum in Figure 2. The continuum level is $<1\sigma$ in the spectrum, so the measured EWs are only lower limits. The lower limit of the rest-frame EW of the Lyα + N V λ1241 emission of J1150+5048 is 921 Å. This is significantly higher than the typical $EW_{Ly\alpha+N\ V}$ at ∼100 Å as indicated by the $EW_{Ly\alpha+N\ V}$ where the number of SDSS quasars is highest in Figure 1.

Figure 3 displays the r-band cutout from HSC-DEX in the upper panels and the narrowband images (±20 Å) of the Lyα, C IV λ1549, He II λ1640 emission lines from HETDEX in the remaining three panels. Only spatial pixels with the signal-to-noise ratio of emission lines greater than 1 are used to generate the narrowband images.

The flux from the Lyα emission-line region is highly spatially resolved in J1150+5048 as shown by the middle panel of Figure 3. The seeing of this HETDEX observation is 1.″6 (FWHM). The

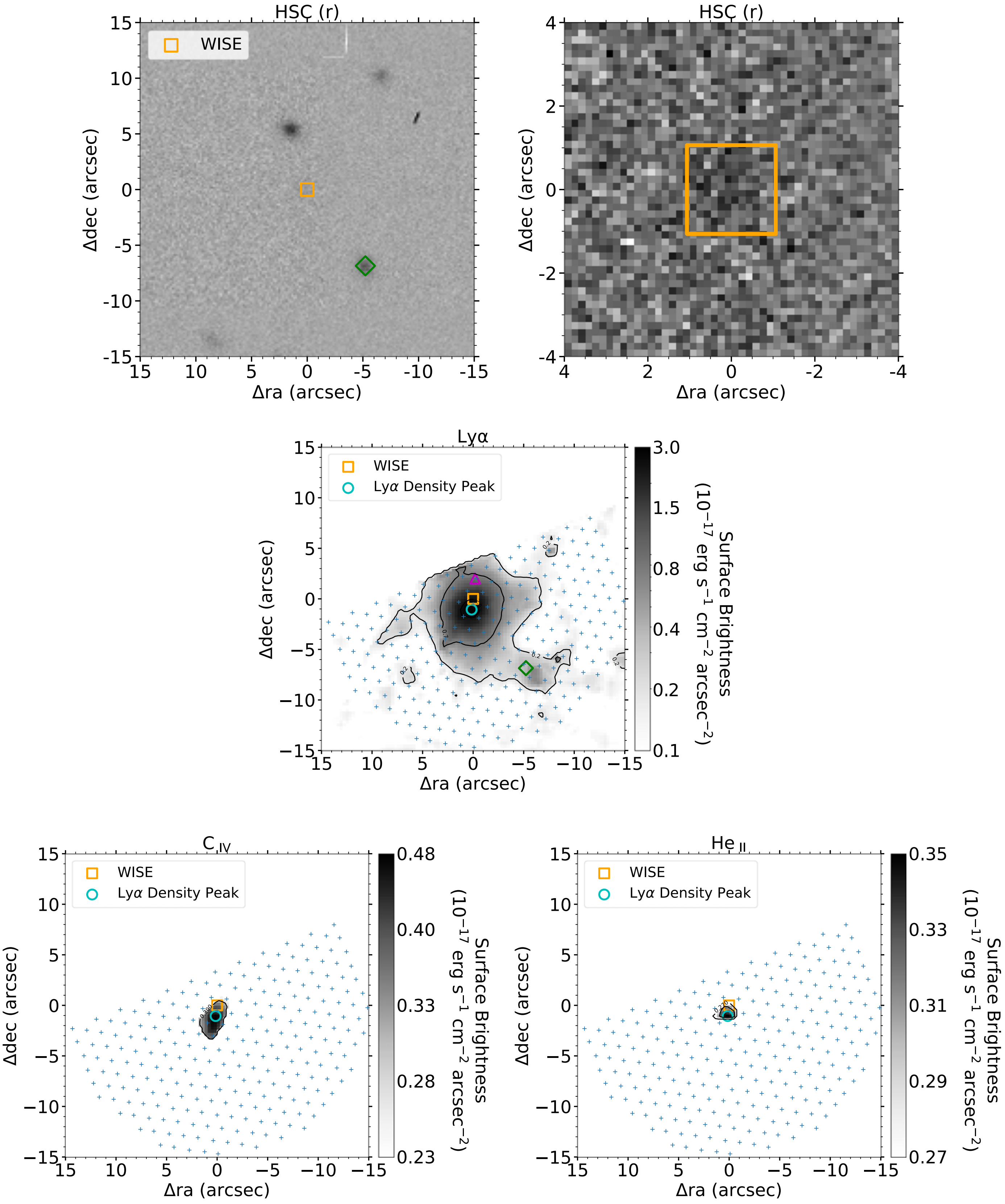

Figure 3. Top panels: the *r*-band image and the expanded version from HSC-DEX. The pointing of the IR detection in the WISE survey is marked with an orange square. The green diamond marks another HSC-DEX *r*-band detection (22.5 mag) that is covered by the HETDEX fibers in this field. Middle panel: the narrowband image of the Lyα emission line derived from the HETDEX data. The small blue plus signs mark the positions of all HETDEX fibers in this field. The cyan circle marks the density peak of the Lyα line, which is also the recorded HETDEX coordinate in Table 1. The magenta triangle is a random position chosen to demonstrate the spatial changes of the Lyα line profiles in Figure 4. Bottom panels: the narrowband images of the C IV λ1549 (left) and He II λ1640 (right) emission lines. The seeing of the HETDEX observation is 1.″6 (FWHM). All images are centered at the coordinate of WISE (continuum center) in Table 1.

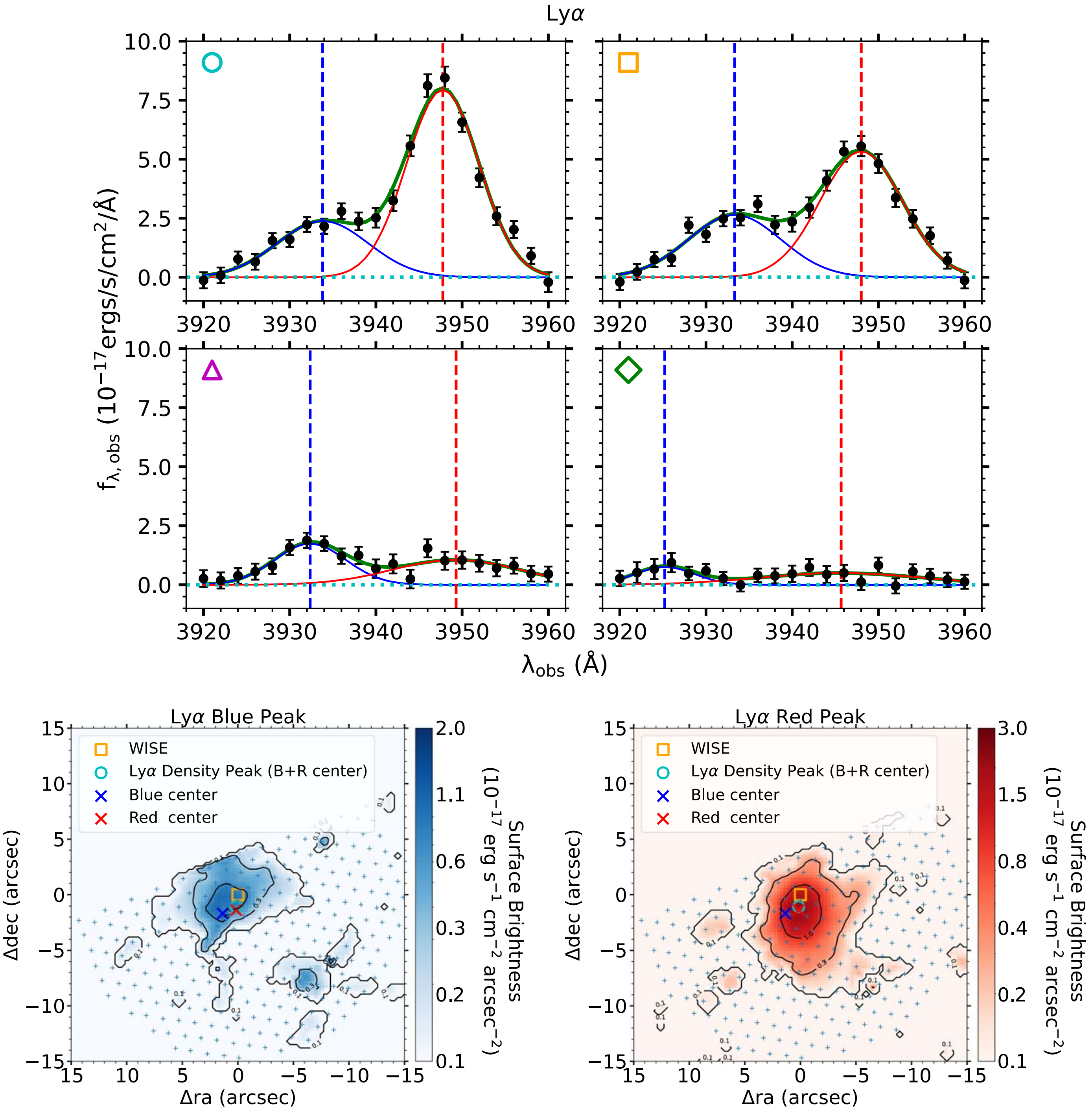

Figure 4. Upper two rows: the spectra of Lyα at the four positions marked by the cyan circle (Lyα density peak), the orange square (the WISE pointing), the magenta triangle (a random position), and the green diamond (another r-band detection) in the narrowband image of the Lyα emission line in Figure 3. Black data points with error bars are the observed spectra. Our best-fit double-Gaussian model is shown by the green curve. The blue and red solid curves are the best-fit blue component and red component. The blue and red vertical lines mark the best-fit central wavelengths of the two peaks. Bottom panels: the surface density map of the spectral decomposed blue peak and red peak of Lyα. The orange square again marks the position of the WISE detection. The blue and the red crosses show the positions where the blue peak and the red peak have the highest line flux respectively.

Lyα emission is clearly more extended than the other two emission lines. It spans a region of $\sim 10''$ (85 kpc) in diameter. The recorded R.A. and decl. of HETDEX in Table 1 is the coordinate where the Lyα line flux is highest (the cyan circle in Figures 3 and 4). The recorded R.A. and decl. of the Wide-field Infrared Survey Explorer (WISE) in Table 1 is the coordinate of the continuum detection, taken from the WISE catalog (Cutri et al. 2021). All images in Figures 3 and 4 are centered at the WISE coordinate. The offset between the emission-line center (HETDEX coordinate) and the continuum center (WISE coordinate) is $1\overset{''}{.}1$.

The emission lines of J1150+5048 are strongly bimodal with a red peak at $z \sim 2.249$ and a blue peak at $z \sim 2.236$ as shown in Figure 4. The recorded redshift of $z \sim 2.24$ in Table 1 is a combination of the red peak and the blue peak.

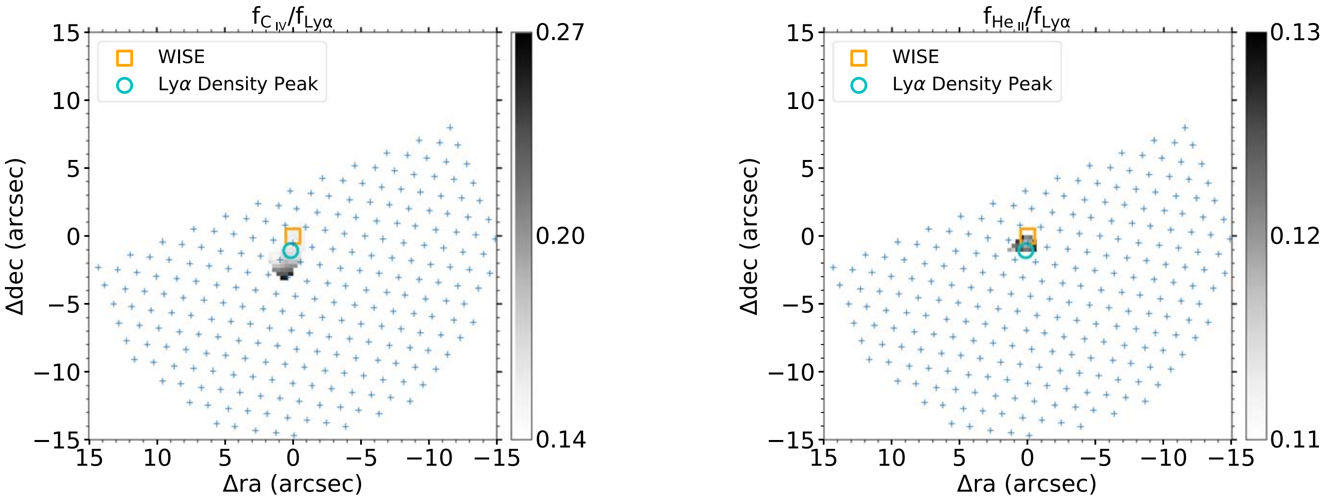

Figure 5. Left: the line flux ratio map of the C IV λ1549 emission over the Lyα emission. Only spatial pixels with both emission lines detected at $>1\sigma$ level are used in the map. Labels are the same with the ones in the narrowband images in Figure 3. Right: similar plot with the left panel, but for the line ratio of the He II λ1640 emission over the Lyα emission.

J1150+5048 is a nondetection ($<1\sigma$) in the g band measured from the HETDEX spectrum at the HETDEX coordinate. It has an IR detection in the WISE catalog (Cutri et al. 2021) with the W4 band (22 μm) being a nondetection. When measuring at the pointing of the IR detection from HSC-DEX, its r-band magnitude is 24.57. The 5σ limiting magnitude of this field is $r = 25.12$. The spatial distribution of the r-band flux of J1150+5048 (top panels in Figure 3) is strikingly different from the typical 24–25 mag sources (see the first two examples of Figure 12 in Paper I): it is so diffuse that it might be dominated by a spatially extended emission line, such as C III] λ1909, rather than the true continuum.

J1150+5048 is a nondetection in the Faint Images of the Radio Sky at Twenty-Centimeters survey (FIRST; Becker et al. 1995), while it has a radio detection at the location of the WISE source at $S_{150\,\mathrm{MHz}} = 2$ mJy from the Low-Frequency Array (LOFAR) Two-meter Sky Survey (LoTSS) (Shimwell et al. 2022).

Figure 4 presents the Lyα line profiles at the four representative positions marked in the Lyα narrowband image of Figure 3 in the upper two rows. The Lyα emission line clearly has two distinctive peaks. We decompose the Lyα emission line into a blue peak and a red peak with a double-Gaussian model. The velocity offset between the two peaks ($\sim$1100 km s^{-1}) does not change significantly with location. The bottom two panels shows the surface density maps of the decomposed blue peak and red peak respectively. The blue cross and the red cross mark the positions where the flux is highest for the blue peak and the red peak. The separation between the two centers is $\sim$1.″2 (10.1 kpc). For most of the spatial pixels, the blue peak is weaker than the red peak. This asymmetry is an evidence of outflows, as the near side of Lyα is resonantly scattered by an optically thick medium. The C IV λ1549 and He II λ1640 emission lines also display double peak profiles; however, the two lines are not sufficiently strong for spatial decomposition as was done for Lyα.

Figure 5 shows the line flux ratio of the C IV λ1549 emission over the Lyα emission in the left panel and that of the He II λ1640 emission over the Lyα emission in the right panel. The line ratio of C IV λ1549/Lyα ranges from 0.1 to 0.3. The line ratio of He II λ1640/Lyα ranges from 0.11 to 0.13. The combination of the C IV λ1549/He II λ1640 ratio and the C III] λ1909/C IV λ1549 would provide diagnostics for the ionization levels and the metallicities given quasar photoionization models (e.g., Guo et al. 2020). Unfortunately, the C III] λ1909 emission is out of the HETDEX wavelength range. Lau et al. (2022) suggested that the the ionization parameter can be assumed to be $\lg U \sim -1$. The C IV λ1549/He II λ1640 ratio of $\sim$1 in at the Lyα density peak (shown by the cyan circle) would suggest a metallicity of $\sim Z_\odot$. The spatially integrated line ratio of $\sim$3 out to $\sim$3″ ($\sim$20 kpc) corresponds to a metallicity of $\sim 0.5\,Z_\odot$. The metallicity enrichment suggests centrally driven outflows to the host galaxy.

4. Discussion

There are several possibilities that can produce the high EW of J1150+5048; we discuss three possible explanations in this section.

4.1. Collapsing Protogiant Elliptical Galaxy

Adams et al. (2009) studied the famous radio-loud AGN (B2 0902+34) at $z = 3.4$ with the VIRUS prototype on the 2.7 m Harlan J. Smith Telescope. B2 0902+34 also has a bimodal Lyα emission-line profile, and the Lyα emission is extended with a radius of $\sim$50 kpc. The observed data was successfully reproduced with a model of a collapsing protogiant elliptical galaxy ($\geqslant 10^{12}\,M_\odot$). $z \sim 2$ is a common era of galaxy formation. Massive galaxies and their formation have many signatures, most of which include a lot of emission in radio and infrared. B2 0902+34 is detected at 300 mJy in the FIRST survey. J1150+5048 is also covered by FIRST, but there is no radio excess within ±30″ of the AGN. The radio detection of J1150+5048 in LoTSS at $S_{150\,\mathrm{MHz}} = 2$ mJy is also too weak compared to B2 0902+34. These may rule out the possibility of collapsing protogiant elliptical galaxy.

4.2. Off-centered SMBH

SMBHs can be ejected after merger event (Loeb 2007; Haiman et al. 2009; Ricarte et al. 2021). If they happen to fall in a gas-rich environment, the ejected SMBH can irradiate the IGM in its vicinity and appear as a naked black hole with no host galaxy. The narrowband emission-line flux maps in Figure 3 show that J1150+5048 might be related with the other

r-band detection covered by the HETDEX fibers marked by the green diamond, which is $r_{\rm AB} = 22.5$ mag. It has weak emission lines at similar redshift with J1150+5048 with a velocity offset of ~ -600 km s^{-1} as shown by the spectra in Figure 4. If the green diamond is the original host and the WISE detection is the SMBH, then the separation between the two is $8\farcs6$ (72 kpc).

4.3. Extremely Red Quasar with Strong Winds

The optical broadband imaging could be heavily obscured by dust in the outskirts of the host galaxy. Extremely red quasars (ERQs) were first identified in Ross et al. (2015) with $r_{\rm AB} - {\rm W4}_{\rm Vega} > 14$ mag, i.e., $r_{\rm AB} - {\rm W4}_{\rm AB} > 7.38$ mag. They were revisited by Hamann et al. (2017) with the definition of $i_{\rm AB} - {\rm W3}_{\rm AB} \geqslant 4.6$ mag and the rest-frame ${\rm EW}_{\rm C\,IV} \geqslant 100$ Å. Although J1150+5048 is a nondetection in the W4 band and it lacks the observation in the i band, the color of $r_{\rm AB} - {\rm W3}_{\rm AB} = 6.93$ mag and high ${\rm EW}_{\rm C\,IV} > 177$ Å indicates that J1150+5048 probably belongs to the ERQ population. The current photometric data are not sufficient to break the degeneracy among various models in the spectral energetic distribution. Photometric observations in more bands, such as the K band and z band, might further help confirm whether J1150+5048 is an ERQ.

Many ERQs are found in large-scale overdensities; we checked the full emission-line catalog of the HETDEX survey (E. M. Cooper et al. 2022, in preparation) and only found one weak Lyα emitter candidate within $\pm 5'$ (2.5 Mpc) at $z = 2.24 \pm 0.03$ down to the detection limit of HETDEX at $g \sim 24.5$ mag. J1150+5048 might not be in a large-scale overdensity.

Besides J1150+5048, we found that other high-EW AGNs in our catalog are all narrow-line AGNs with FWHM ~ 1000 km s^{-1}, corresponding to the velocity dispersion of $\sim$400 km s^{-1}. Lau et al. (2022) also found that the Lyα halo of the ERQ they studied is kinematically quiet with the velocity dispersion of $\sim$300 km s^{-1}.

A significant fraction of our AGN sample has extended emission-line regions. Ouchi et al. (2020) collected emitters with measurements of their diffuse Lyα emission and found that the radius of diffuse Lyα emitters are correlated with the Lyα luminosities. The Lyα luminosity of their sample ranges from $\sim 10^{42}$ to $\sim 10^{45}$ erg s^{-1}. The spatially integrated Lyα luminosity of J1150+5048 is $10^{43.4}$ erg s^{-1}. The Lyα emission of J1150+5048 extends to $r \sim 85$ kpc. J1150+5048 lies well within the scattered region of the correlation between the radius and the Lyα luminosity in Figure 13 of Ouchi et al. (2020).

The extended emission-line region can be explained either by central-driven outflows or by inflows from the circumgalactic medium. The blue peak of the Lyα emission is always weaker than the red peak. This suggests that the near side is more heavily scattered than the far side, and the gas flows are outflows rather than inflows. If the direction of the outflows are perpendicular to the line-of-sight direction, the separation between the blue peak and the red peak ($\sim$1100 km s^{-1}) would not change significantly with positions as was found in Section 3.

We estimate the outflow mass $M_{\rm outflow}$ and the outflow rate $\dot{M}_{\rm outflow}$ of J1150+5048 following Equations (5) and (6) in Fluetsch et al. (2021). However, the Hα emission is not covered by the wavelength range of the HETDEX spectrum. We therefore make a simple assumption that the luminosity of the Lyα emission is around 1.5 times that of the Hα emission following (Allen et al. 1982). The electron density n_e should be carefully calculated from doublets such as the [O II] λ3726/[O II] λ3729 ratio and the [S II] λ6717/[S II] λ6731 ratio, but these emission lines are again out of the wavelength coverage of HETDEX. We then take the typical n_e of outflows $\sim$500 cm^{-3} from Fluetsch et al. (2021). With these two assumptions, the outflow mass and the outflow rate of J1150+5048 are then $\lg(M_{\rm outflow}/M_\odot) \sim 8$ and 1.5 $M_\odot$ yr^{-1}.

As shown in Figure 1, there are many other high-EW AGNs in our catalog, although some are missing r-band imaging, and some do not have significant emission lines detected besides Lyα. By the time the HETDEX survey is complete, we expect the final AGN sample to be about 5 times larger than the current one. We will systematically study all AGNs with high EWs. It is expected that many of these high-EW AGNs are similar to J1150+5048 with red colors and bipolar outflows. It is interesting to study the outflow properties, such as the outflow mass $M_{\rm outflow}$ and the outflow rate $\dot{M}_{\rm outflow}$, as a function of luminosity, reddening, and redshift.

5. Summary

We have identified an AGN (J1150+5048) with an extremely high EW at $z \sim 2.24$, with strong Lyα, C IV λ1549, and He II λ1640 emission lines and nondetected continuum in the HETDEX spectrum. The measured ${\rm EW}_{\rm Ly\alpha+N\,V,rest} = 921$ Å is a lower limit of its rest-frame line strength at Lyα. Extended emission is measured at $r = 24.57$ in the deep r-band image ($r_{5\sigma} = 25.12$) from the HSC-DEX survey. It has an IR detection in the WISE catalog, but it is a nondetection in the W4 band. The Lyα emission line is significantly extended in the narrowband image spanning $\sim 10''$ in diameter in the observation. The line profile of Lyα is strongly bimodal. The decomposed blue peak and red peak separated from each other with $1\farcs2$. The line-of-sight velocity offset between the two peaks is $\sim$1100 km s^{-1}.

Further statistical studies on the full high-EW AGN sample are needed to understand the relation among this sample, the ERQs, type-II AGNs, and the AGNs with diffuse ionized gas. These would provide key information for understanding the early quasar phases, galaxy quenching, and the enrichment of the IGM. The HETDEX survey is very efficient in such studies because the spatial resolved information is observed simultaneously while the emission-line sources are identified in the 18 minute spectroscopic exposures with no preselection based on imaging.

HETDEX is led by the University of Texas at Austin McDonald Observatory and Department of Astronomy with participation from the Ludwig-Maximilians-Universität München, Max-Planck-Institut für Extraterrestrische Physik (MPE), Leibniz-Institut für Astrophysik Potsdam (AIP), Texas A&M University, The Pennsylvania State University, Institut für Astrophysik Göttingen, The University of Oxford, Max-Planck-Institut für Astrophysik (MPA), The University of Tokyo, and Missouri University of Science and Technology. In addition to Institutional support, HETDEX is funded by the National Science Foundation (grant AST-0926815), the State of Texas, the US Air Force (AFRL FA9451-04-2-0355), and generous support from private individuals and foundations.

The Hobby–Eberly Telescope (HET) is a joint project of the University of Texas at Austin, the Pennsylvania State University, Ludwig-Maximilians-Universität München, and Georg-August-Universität Göttingen. The HET is named in honor of its principal benefactors, William P. Hobby and Robert E. Eberly.

The authors acknowledge the Texas Advanced Computing Center (TACC) at The University of Texas at Austin for providing high performance computing, visualization, and storage resources that have contributed to the research results reported within this paper. URL: http://www.tacc.utexas.edu.

ORCID iDs

Chenxu Liu https://orcid.org/0000-0001-5561-2010
Karl Gebhardt https://orcid.org/0000-0002-8433-8185
Wolfram Kollatschny https://orcid.org/0000-0002-0417-1494
Robin Ciardullo https://orcid.org/0000-0002-1328-0211
Erin Mentuch Cooper https://orcid.org/0000-0002-2307-0146
Dustin Davis https://orcid.org/0000-0002-8925-9769
Daniel J. Farrow https://orcid.org/0000-0003-2575-0652
Steven L. Finkelstein https://orcid.org/0000-0001-8519-1130
Eric Gawiser https://orcid.org/0000-0003-1530-8713
Caryl Gronwall https://orcid.org/0000-0001-6842-2371
Gary J. Hill https://orcid.org/0000-0001-6717-7685
Lindsay House https://orcid.org/0000-0002-1496-6514
Donald P. Schneider https://orcid.org/0000-0001-7240-7449
Tanya Urrutia https://orcid.org/0000-0001-6746-9936
Gregory R. Zeimann https://orcid.org/0000-0003-2307-0629

References

Adams, J. J., Hill, G. J., & MacQueen, P. J. 2009, ApJ, 694, 314
Aihara, H., AlSayyad, Y., Ando, M., et al. 2019, PASJ, 71, 114
Allen, D. A., Barton, J. R., Gillingham, P. R., & Carswell, R. F. 1982, MNRAS, 200, 271
Bahcall, J. N., Kirhakos, S., & Schneider, D. P. 1994, ApJL, 435, L11
Becker, R. H., White, R. L., & Helfand, D. J. 1995, ApJ, 450, 559
Cai, Z., Fan, X., Yang, Y., et al. 2017, ApJ, 837, 71
Cutri, R. M., Wright, E. L., Conrow, T., et al. 2021, yCat, 2328
Fluetsch, A., Maiolino, R., Carniani, S., et al. 2021, MNRAS, 505, 5753
Gebhardt, K., Mentuch Cooper, E., Ciardullo, R., et al. 2021, ApJ, 923, 217
Guo, Y., Maiolino, R., Jiang, L., et al. 2020, ApJ, 898, 26
Haiman, Z., Kocsis, B., & Menou, K. 2009, ApJ, 700, 1952
Hamann, F., Zakamska, N. L., Ross, N., et al. 2017, MNRAS, 464, 3431
Hill, G. J., Lee, H., MacQueen, P. J., et al. 2021, AJ, 162, 298
Kormendy, J., & Ho, L. C. 2013, ARA&A, 51, 511
Lau, M. W., Hamann, F., Gillette, J., et al. 2022, MNRAS, 515, 1624
Liu, C., Gebhardt, K., Mentuch Cooper, E., et al. 2022, ApJS, 261, 24
Loeb, A. 2007, PhRvL, 99, 041103
Luo, B., Brandt, W. N., Xue, Y. Q., et al. 2017, ApJS, 228, 2
McIntosh, D. H., Rieke, M. J., Rix, H. W., Foltz, C. B., & Weymann, R. J. 1999, ApJ, 514, 40
McLure, R. J., Kukula, M. J., Dunlop, J. S., et al. 1999, MNRAS, 308, 377
Ouchi, M., Ono, Y., & Shibuya, T. 2020, ARA&A, 58, 617
Pâris, I., Petitjean, P., Aubourg, É., et al. 2018, A&A, 613, A51
Rakshit, S., Stalin, C. S., & Kotilainen, J. 2020, ApJS, 249, 17
Ricarte, A., Tremmel, M., Natarajan, P., Zimmer, C., & Quinn, T. 2021, MNRAS, 503, 6098
Richards, G. T., Strauss, M. A., Fan, X., et al. 2006, AJ, 131, 2766
Ross, N. P., Hamann, F., Zakamska, N. L., et al. 2015, MNRAS, 453, 3932
Shimwell, T. W., Hardcastle, M. J., Tasse, C., et al. 2022, A&A, 659, A1
Stern, D., Assef, R. J., Benford, D. J., et al. 2012, ApJ, 753, 30
Vayner, A., Zakamska, N. L., Riffel, R. A., et al. 2021, MNRAS, 504, 4445
Xue, Y. Q., Luo, B., Brandt, W. N., et al. 2016, ApJS, 224, 15